PHYSICAL REVIEW APPLIED **16,** 054034 (2021)

Toward Hole-Spin Qubits in Si *p*-MOSFETs within a Planar CMOS Foundry Technology

L. Bellentani,[1] M. Bina,[2] S. Bonen,[3] A. Secchi,[1,*] A. Bertoni,[1] S. P. Voinigescu,[3] A. Padovani,[2]
L. Larcher,[2] and F. Troiani[1]

[1] *Centro S3, CNR-Istituto di Nanoscienze, via G. Campi 213/A, I-41125 Modena, Italy*
[2] *Applied Materials—MDLx Italy R&D, 42124 Reggio Emilia, Italy*
[3] *Edward S. Rogers Snr. Department of Electrical and Computer Engineering, University of Toronto, Toronto, Ontario M5S 3G8, Canada*

(Received 14 June 2021; revised 20 September 2021; accepted 18 October 2021; published 17 November 2021)

Hole spins in semiconductor quantum dots represent a viable route for the implementation of electrically controlled qubits. In particular, the qubit implementation based on Si *p*-MOSFETs offers great potentialities in terms of integration with the control electronics and long-term scalability. Moreover, the future down scaling of these devices will possibly improve the performance of both the classical (control) and quantum components of such monolithically integrated circuits. Here, we use a multiscale approach to simulate a hole-spin qubit in a down-scaled Si-channel *p*-MOSFET, the structure of which is based on a commercial 22-nm fully depleted silicon-on-insulator device. Our calculations show the formation of well-defined hole quantum dots within the Si channel and the possibility of a general electrical control, with Rabi frequencies of the order of 100 MHz for realistic field values. A crucial role of the channel aspect ratio is also demonstrated, as well as the presence of a favorable parameter range for the qubit manipulation.

DOI: 10.1103/PhysRevApplied.16.054034

I. INTRODUCTION

Localized spins in semiconductors were recognized early on as one of the most promising means for the encoding and manipulation of quantum information [1]. In the past decade, this approach has gained renewed interest, due to the high degree of control achieved on the single- and few-particle states in Si [2] and Ge quantum dots [3]. Within this platform, all the fundamental criteria for the implementation of quantum computation have recently been met, from high-fidelity one- [4–6] and two-qubit gates [7–9] to qubit readout [10–12] and coherent spin transfer [13,14]. Crucially, carrier spins in Si and Ge benefit from long coherence times [15], due to the limited impact of hyperfine interactions, which, instead, represent a ubiquitous source of decoherence in III–V compounds. Besides, Si and Ge represent key materials in modern electronics and thus provide a common platform for integrating qubits and control circuits [16–18].

As regards scalability, a fundamental advantage of the semiconductor-based approach would be represented by the use of homogeneous building blocks for realizing both the quantum (qubits) and classical (control electronics) components of the hardware. This route has been undertaken with the implementation of complementary-metal–oxide–semiconductor (CMOS) qubits, obtained by suitably modifying transistors currently fabricated in foundry processes [12,16,19–22]. In particular, hole spins in group-IV materials offer strong spin-orbit coupling, which enables all-electric qubit manipulation, thus avoiding the introduction in the circuit design of elements that are incompatible with the industrial fabrication processes [3,19,23–32].

One of the key challenges in this direction is to find a trade-off amongst the conflicting requirements of operating the qubits at millikelvin temperatures, in order to enhance the coherence times, and the control electronics at higher temperatures (at least 1–4 K), in order to allow a sufficiently fast removal of the dissipated power [33–37]. In this respect, a crucial role might be played by the qubit implementation in down-scaled MOSFETs, which would improve the efficiency of the control and readout electronics and enhance, with the quantum confinement, the temperatures and frequencies at which the qubits can be operated.

In this paper, we perform a multiscale simulation of fully depleted silicon-on-insulator *p*-MOSFETs, which represents a down-scaled version of the 22-nm commercial devices. The technology computer-aided design (TCAD) simulation of the devices allows us to account for the

---

[*] andrea.secchi@nano.cnr.it

material properties, doping profile, and electrical parameters in the device and to derive realistic profiles for the confining potential in the low-temperature regime. The hole states are then computed within a six-band $\mathbf{k}\cdot\mathbf{p}$ approach, in order to derive the quantities that define the properties and functionalities of the spin qubit. Our simulations show that the considered device geometry allows the formation of a well-defined quantum dot, entirely localized at the center of the Si channel. Besides, the application to the top gate of different voltage pulses enables the implementation of spin-qubit rotations around all three axes of the Bloch sphere, with Rabi frequencies of the order of 10^2 MHz. We determine the dependence of such Rabi frequencies on the orientation of the static magnetic field and find a trade-off between optimizing longitudinal and transverse rotations. Finally, we identify the optimal aspect ratio of the Si channel, which corresponds to the occurrence of a clear transition in the ground-state properties.

The paper is organized as follows. Section II is devoted to the modeling of the scaled p-MOSFET and to the calculation of the confining potentials. In Sec. II, we characterize the hole states in terms of spatial symmetry and localization in the device, band mixing, and interlevel spacing. The dependence of the Rabi frequencies on the magnetic field (intensity and orientation) and on the geometry of the silicon channel are discussed in Sec. IV and Sec. V, respectively. The conclusions are drawn in Sec. VI, while further details on the method are provided in Appendices A–D.

II. THE SILICON p-MOSFET

The devices that we consider [Fig. 1(a)] represent scaled p-MOSFET versions of those already fabricated in the GlobalFoundries 22-nm fully depleted silicon-on-insulator (FDSOI) process [38]. The possibility of monolithic integration between qubits and high-fidelity readout circuitry at 2 K in production 22-nm FDSOI CMOS technology has recently been demonstrated [21]. The further scaling of the transistor minimum feature size represents a precondition for operating the qubits at high temperatures and control frequencies.

The quantum dot is formed in the thin undoped semiconductor film below the top gate. The shallow-trench isolation oxides on the two sides of the Si channel (y direction) and the top-gate oxides and buried oxides (z direction) form almost infinite potential barrier wells with dimensions $W = 10$ nm and $H = 5$ nm, respectively [see Fig. 1(d)]. The confinement along the x direction results from the combined effect of the top- and back-gate voltages (V_G and V_B) of the nitride spacers and of the nonuniform p-type doping in the source-drain (S-D) regions.

In more detail, the high-κ metal-gate stack (length $L_G = 10$ nm) consists of a 1-nm SiO_2 interfacial layer and a 1.5-nm HfO_2 layer; the metal contact on top is simulated by a TiN interface with a 4.57-eV work function. The stack is separated from the S-D contacts (length $L_s = 10$ nm) by 3-nm Si_3N_4 spacers [see Figs. 1(b) and 1(c)]. The S-D regions are simulated by realistic nonuniform p-type doping distributions, consisting of a Gaussian profile along the z direction, a uniform profile (with a Gaussian edge) along the x direction, and a peak of the acceptor doping concentration of -10^{20} cm^{-3}. The Si channel (with an n-type donor concentration of 10^{15} cm^{-3}) is thus formed between the top gate and the (20-nm-thick) SiO_2 buried oxide and delimited by the S-D doped regions [see Fig. 1(e)].

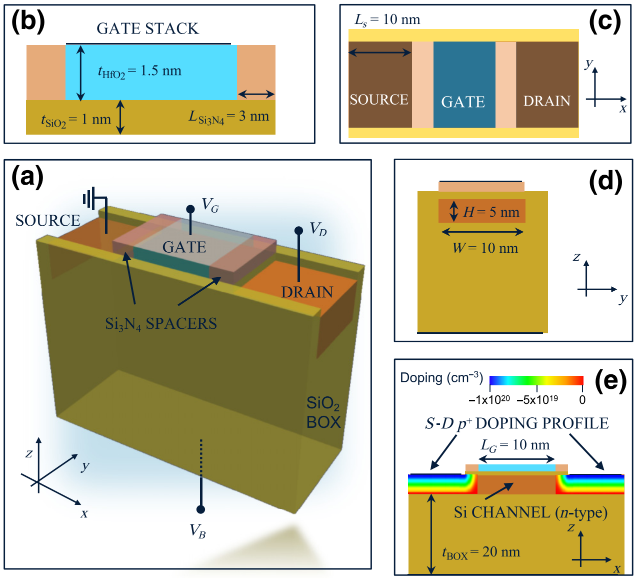

FIG. 1. (a) The schematics of the simulated p-MOSFET FDSOI transistor. (b) The composition and geometry of the high-κ metal-gate stack. (c)–(e) Top (c), side (d), and front (e) views of the device; in the latter, we highlight the nonuniform Gaussian-doping profile in the source and drain.

The simulation of this device is carried out by a multiscale approach [39–42]. The geometry and composition of the device are estimated from Ref. [38], on the basis of scaling laws. The device is simulated with the GINESTRA® simulation software. This allows us to determine the three-dimensional (3D) potential energy profile that confines the holes and defines the quantum dot, starting from the device geometry and material properties, through a self-consistent description of charge transport (see Appendix A). Crucially, the GINESTRA software has the capability to simulate the device physics at the temperature $T = 2$ K.

A representative example of the confining potentials $U(\mathbf{r})$ generated in the p-MOSFET for different values of the top-gate potential V_G and a channel width $W = 10$ nm is reported in Fig. 2. At zero S-D bias and for a back-gate voltage $V_B = 0.5$ V, a hole quantum dot is clearly formed in the Si channel, as a combined effect of the band offsets at the Si/SiO_2 interfaces and of the electrostatic potential

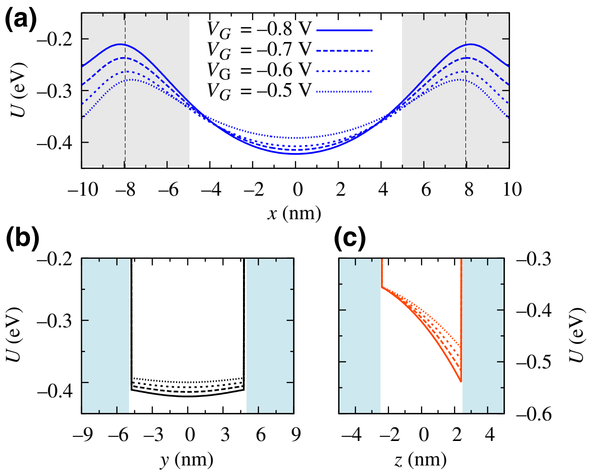

FIG. 2. The confining potential $U(\mathbf{r})$ induced by the top and back gates along the symmetry axes of the silicon channel: (a) $y = z = 0$ nm, (b) $x = z = 0$ nm, and (c) $x = y = 0$ nm. In (a), the shaded areas ($|x| \geq 4.98$ nm) correspond to the source and drain regions, while the dotted lines delimit the region below the nitride spacers ($7.96 \text{ nm} \geq |x| \geq 4.98$ nm). In (b) and (c), the shaded areas identify the SiO_2 regions ($|y| \geq 5$ nm and $|z| \geq 2.5$ nm, respectively). The device temperature in the simulation is $T = 2$ K.

induced by the gates. In particular, the band offset at the Si/SiO_2 interface produces sharp confining barriers in the y and z directions [see Figs. 2(b) and 2(c)]. The applied voltage induces a potential gradient along z, which tends to localize the holes close to the top gate. The potential profile is qualitatively different (much smoother) along the channel direction (x). Here, the top gate induces a central minimum, separated from the doped *S*-*D* regions by two tunneling barriers. The depth of the minimum increases for decreasing values of the gate voltage V_G, which can be varied within a significant range of values, thus allowing the tuning of the qubit properties (see below). The formation of a well-defined quantum dot in the center of Si channel is obtained for $V_G \lesssim -0.3$ V. However, in order to remain safely within the required confinement regime, we focus hereafter on more negative values of the gate voltage. Further details on the TCAD simulations are reported in Appendix A.

III. HOLE STATES

The confining potential $U(\mathbf{r})$ generated by the TCAD simulations represents the starting point for the calculation of the hole eigenstates, which is performed by diagonalizing a six-band Lüttinger-Kohn envelope-function Hamiltonian $H_{\mathbf{k}\cdot\mathbf{p}}$ [43] (see Appendix B). The hole eigenstates, which at zero magnetic field form degenerate Kramers doublets, are denoted hereafter using

$$|m, \xi\rangle = \sum_b \sum_{\mathbf{n}} c_{m,\xi}^{\mathbf{n},b} |\mathbf{n}, b\rangle. \tag{1}$$

Here, the index $m \geq 1$ specifies the doublet and $\xi = \Uparrow, \Downarrow$ the individual eigenstate. The eigenstates are expanded on a basis of band-orbital states specified by the indexes $\mathbf{n}$ and b. The band index, $b \equiv (J, M)$, distinguishes between heavy-hole $(3/2, \pm 3/2)$, light-hole $(3/2, \pm 1/2)$, and split-off $(1/2, \pm 1/2)$ bands. The orbital index $\mathbf{n} \equiv (n_x, n_y, n_z)$ specifies a set of 3D harmonic oscillator states, on which the envelope functions are expanded.

The qubit initialization and manipulation requires the application of a static magnetic field $\mathbf{B} = B(\cos\theta \cos\phi, \cos\theta \sin\phi, \sin\theta)$, the coupling of which with the confined holes is described by a Hamiltonian H_B, which includes the Zeeman ($H_{B,Z}$), the paramagnetic ($H_{B,P}$), and the diamagnetic ($H_{B,D}$) terms (see Appendix B). The field removes the degeneracy within each Kramers doublet and thus defines unambiguously the pair of eigenstates $|m, \xi\rangle$, which depend on the field orientation (θ, ϕ) and intensity (B).

In the remainder of this Section, we discuss the properties of the hole states for a prototypical scaled p-MOSFET device with channel width $W = 10$ nm. The dependence of the hole properties on the channel width is discussed in Sec. V.

A. Quantum dot formation

The actual formation of a hole quantum dot implies the 3D localization within the Si channel of (at least) the hole ground states $|1, \xi\rangle$ ($\xi = \Uparrow, \Downarrow$), which is indeed achieved in the case considered (Fig. 3).

In order to quantify the degree of localization for the lowest hole eigenstates, we compute their penetration probabilities in the oxide barriers ($\mathcal{R}_{\text{Ox}}$), in the entire *S*-*D* region ($\mathcal{R}_{SD}$), and specifically below the nitride spacers ($\mathcal{R}_{\text{NS}} \subset \mathcal{R}_{SD}$). For the generic region $\mathcal{R}$ and the eigenstate $|m, \xi\rangle$, the penetration probability reads as follows:

$$p_m(\mathcal{R}) = \int_{\mathcal{R}} d\mathbf{r}\, |\langle \mathbf{r} | m, \xi \rangle|^2. \tag{2}$$

These probabilities are independent of $\xi = \Uparrow, \Downarrow$ at zero magnetic field and display a negligible dependence on $\mathbf{B}$ in the considered range of field values. Their values are at most of the order of 1% for the states belonging to the ground doublet (Table I) and only slightly larger for the first eight excited states (not reported here). Most of the leakage takes place along the x direction, toward the source and drain; in particular, in the region below the nitride spacers. The hole confinement is stronger in the y and z directions, where the large band offset between Si and SiO_2 limits the leakage probabilities to less than 0.2%. The

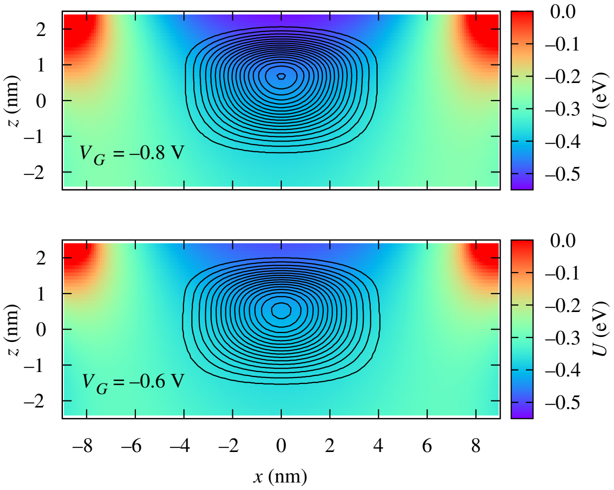

FIG. 3. A map of the confining potential $U(\mathbf{r})$ at $y = 0$ nm, for different values of the gate potential ($V_G = -0.8$ V and $V_G = -0.6$ V in the top and bottom panels, respectively). The black contour lines show the charge density $\rho_{1,\xi}(\mathbf{r}) = |\langle \mathbf{r}|1,\xi\rangle|^2$, corresponding to the hole ground states at zero magnetic field, from a value of 0.1 (outer line) to 0.95 (inner line), with an incremental step of 0.05 (all in atomic units).

comparison between the probabilities corresponding to different values of V_G shows a clear dependence of $p(\mathcal{R}_{SD})$ and $p(\mathcal{R}_{\rm NS})$ on the top-gate voltage, which has, instead, a limited impact on $p(\mathcal{R}_{\rm Ox})$.

The energy separation ΔE between the ground and the first excited doublet quantifies the strength of the quantum confinement in the dot and thus provides an estimate of the highest temperature at which its effects can be observed. Here, such a gap is given by $\Delta = 6.58$ (6.95) meV at $V_G = -0.8$ (-0.6) V, which corresponds to a temperature of $T = \Delta/k_B = 76.358$ (80.651) K. Overall, this shows the possibility of obtaining well-defined quantum dots within the present geometry, with strongly confined hole states.

TABLE I. The characterization of the hole ground state in terms of wave-function localization, symmetries, and band occupation (upper, middle, and lower panels, respectively). In particular, the penetration probabilities refer to the *S*-*D* regions ($\mathcal{R}_{SD}$, corresponding to 10 nm $\geq |x| \geq$ 4.98 nm), below the nitride spacers ($\mathcal{R}_{\rm NS}$, 7.96 nm $\geq |x| \geq$ 4.98 nm), and of the oxides that confine the holes along the y ($\mathcal{R}^y_{\rm Ox}$, 8.4 nm $\geq |y| \geq$ 5.04 nm) and z ($\mathcal{R}^z_{\rm Ox}$, 3.5 nm $\geq |z| \geq$ 2.5 nm) directions.

V_G (V)	$p(\mathcal{R}_{SD})$ (%)	$p(\mathcal{R}_{\rm NS})$ (%)	$p(\mathcal{R}^y_{\rm Ox})$ (%)	$p(\mathcal{R}^z_{\rm Ox})$ (%)
−0.8	0.91	0.77	0.01	0.19
−0.6	1.42	1.23	0.01	0.18
V_G (V)	$p^{hh}_{1,\xi}$ (%)	$p^{lh}_{1,\xi}$ (%)	$p^{so}_{1,\xi}$ (%)	
−0.8	86.44	11.57	1.99	
−0.6	83.14	14.56	2.30	
V_G (V)	$\langle\sigma_{yz}\rangle$	$\langle\sigma_{zx}\rangle$	$\langle\sigma_{xy}\rangle$	$\langle\sigma_r\rangle$
−0.8	0.9655	0.9670	0.8548	0.8870
−0.6	0.9550	0.9692	0.8894	0.9289

Holes in Si are characterized by a large effective mass with respect to Ge. This affects interdot tunneling [44], resulting in fabrication constraints on the gate length and on the dot uniformity. Possible solutions to these problems include the exploitation of excited orbitals and band mixing. In fact, on the one hand, the interdot distance that allows a tunnel coupling between adjacent dots can be increased by the use of excited orbitals in multihole states, rather than the ground orbital in singly occupied dots. The same effect can be produced by the enhancement of the in-plane light-hole component, through the tuning of the confining potential (the geometry, composition, and applied gate voltages) and the strain. As for the nonuniformity of the dots within an array, the FDSOI technology specifically offers a possible solution, namely the use of the back gate as a means of tuning the energy levels within each dot.

B. Band mixing

The mixing between the subbands affects a number of relevant properties of the hole qubit and represents a prerequisite for its manipulation by means of electric fields [45]. In order to quantify such mixing, we refer in the following to the probabilities

$$P^{\chi}_{m,\xi} = \sum_{b\in\chi} p^{b}_{m,\xi} = \sum_{b\in\chi}\left(\sum_{\mathbf{n}} |c^{\mathbf{n},b}_{m,\xi}|^2\right), \tag{3}$$

which give the weights, for the hole eigenstate $|m,\xi\rangle$, of the heavy-hole ($\chi = hh$), light-hole ($\chi = lh$), and split-off bands ($\chi = so$). In the weak-field limit, where the magnetic field does not induce a significant mixing between states belonging to different doublets, we have that $P^{\chi}_{m,\Uparrow} = P^{\chi}_{m,\Downarrow}$ and these probabilities are independent of the field orientation (while this is not the case for the individual-band probabilities $p^{b}_{m,\xi}$).

In all the considered cases, the ground state presents a largely heavy-hole character but also a significant occupation of the light-hole subbands, corresponding to values of $p^{lh}_{1,\xi}$ larger than 10%, as reported in Table I. This results from the fact that the strength of the vertical (z) confinement is comparable to that in the x and (especially) y directions (see Fig. 2). The split-off band presents a limited weight ($p^{so}_{1,\xi} \lesssim 2\%$). However, it provides an indirect coupling between the heavy- and light-hole subbands, which significantly affects their occupation probabilities. Its inclusion in the calculation is thus required in order to get an accurate description of the hole eigenstates. In particular, this applies to the Rabi frequencies, which are extremely sensitive to small changes in the mixing between the heavy and light holes (see Sec. IV).

C. Wave-function symmetry

One additional feature plays a role in the manipulation of the hole-spin qubit, namely the symmetry of the ground-state wave function. As shown in Fig. 3, the charge density in the ground state is asymmetric in the z direction (the hole is attracted toward the top gate) and approximately symmetric along the x and y axes. A more precise and quantitative characterization of the eigenstate symmetry is obtained by computing the expectation values of the operators $\sigma_{\alpha\beta}$, which implement a reflection of the wave-function envelope in the α-β plane (where α-β represents x-y, y-z, or z-x), and σ_r, which implements a spatial inversion ($\mathbf{r} \rightarrow -\mathbf{r}$). Their expectation values can be directly deduced from the symmetry properties of the basis states and are given by

$$\langle m, \xi | \sigma_{\alpha\beta} | m, \xi \rangle = \sum_b \sum_{\mathbf{n}} |c_{m,\xi}^{b,\mathbf{n}}|^2 (-1)^{n_\gamma} \tag{4}$$

(where $\gamma \neq \alpha, \beta$) and

$$\langle m, \xi | \sigma_r | m, \xi \rangle = \sum_b \sum_{\mathbf{n}} |c_{m,\xi}^{b,\mathbf{n}}|^2 (-1)^{n_x+n_y+n_z}. \tag{5}$$

The expectation values of the symmetry operators introduced above are between -1 and $+1$, where the extremal values denote that the hole eigenstate has a complete odd or even symmetry, respectively. An intermediate value signals that the hole eigenstate is an admixture of odd and even orbital states.

The ground state is only approximately symmetric in all directions (Table I). In fact, non-negligible deviations of the expectation values from 1 are obtained, especially for σ_{xy} and σ_r. The value of $\langle \sigma_{xy} \rangle$ decreases for decreasing values of V_G, thus reflecting the relative relevance in the z confinement of the oxide barriers (which are symmetric) and of the gate voltage (approximately antisymmetric). The smaller deviations from 1 of $\langle \sigma_{yz} \rangle$ and $\langle \sigma_{zx} \rangle$ result from the light-hole component of the ground state and are due to the band-mixing (off-diagonal) terms in $H_{\mathbf{k}\cdot\mathbf{p}}$. In general, a lower degree of symmetry of the hole ground state and/or in the spatial profile of the manipulating electric fields represents a potential advantage in terms of qubit manipulation capabilities, for it reduces the symmetry-related selection rules that have to be fulfilled in order to induce the desired transitions [46].

IV. LARMOR AND RABI FREQUENCIES

The static magnetic field $\mathbf{B}$ plays a fundamental role in the initialization and manipulation of the hole-spin qubit. In fact, it opens a gap between the two (otherwise degenerate) ground states $|1, \Uparrow\rangle$ and $|1, \Downarrow\rangle$ and thus determines the Larmor frequency,

$$f_L = \frac{1}{h} \left(E_{1,\Uparrow} - E_{1,\Downarrow} \right), \tag{6}$$

at which the spin manipulation has to be performed by means of oscillating fields. Besides, it affects the band mixing in the ground states, and creates the possibility of inducing transitions between them through electric fields. Within the present geometry, the spin-qubit manipulation is performed by means of time-dependent voltages applied to the top gate (Fig. 1). In order to assess the possibility of implementing arbitrary single-qubit gates, we compute hereafter the Rabi frequencies, corresponding to unitary transformations that are either diagonal or off-diagonal in the eigenstate basis.

Transverse rotations are identified here with unitary transformations $\exp(-i\varphi_X \sigma_X/2)$, where σ_X is the first Pauli matrix (expressed in the $\{|1, \Downarrow\rangle, |1, \Uparrow\rangle\}$ basis) and they allow transitions between the qubit eigenstates. Physically, such rotations are implemented by a resonant ac voltage $\delta V_G \cos(f_L t)$ and are characterized by the Rabi frequency:

$$f_R^X = \frac{1}{h} |\langle 1, \Uparrow | \delta U | 1, \Downarrow \rangle|, \tag{7}$$

where $\delta U(\mathbf{r}) = U_{V_G+\delta V_G}(\mathbf{r}) - U_{V_G}(\mathbf{r})$ is the difference between the confining potentials corresponding to the gate voltages $V_G + \delta V_G$ and V_G.

Longitudinal rotations correspond to unitary transformations $\exp(-i\varphi_Z \sigma_Z/2)$ and modify the relative phase of the qubit eigenstates. Physically, this is obtained by modulating the energy gap between the two basis states through a dc voltage δV_G. The corresponding Rabi frequency is given by

$$f_R^Z = \frac{1}{2h} |\langle 1, \Uparrow | \delta U | 1, \Uparrow \rangle - \langle 1, \Downarrow | \delta U | 1, \Downarrow \rangle|. \tag{8}$$

In general, it is not possible to selectively turn on, through the time-dependent voltage, either the diagonal ($\xi = \xi'$) or the off-diagonal elements ($\xi \neq \xi'$) of the differential potential matrix $\langle 1, \xi | \delta U | 1, \xi' \rangle$. However, the modulation of the diagonal elements can be neglected while considering rotations around the X axis, because it takes place at a frequency $f_L \gg f_R^Z$ and thus averages to zero during the ac voltage pulse (in the spirit of the rotating-wave approximation). Analogously, the off-diagonal elements of δU do not affect the rotations around the Z axis, because they are much smaller than the difference between the diagonal ones ($f_L \gg f_R^X$).

A. Dependence of the Rabi frequencies on the magnetic field intensity

The electric field cannot directly couple two states that are conjugated by time-reversal symmetry, as is the

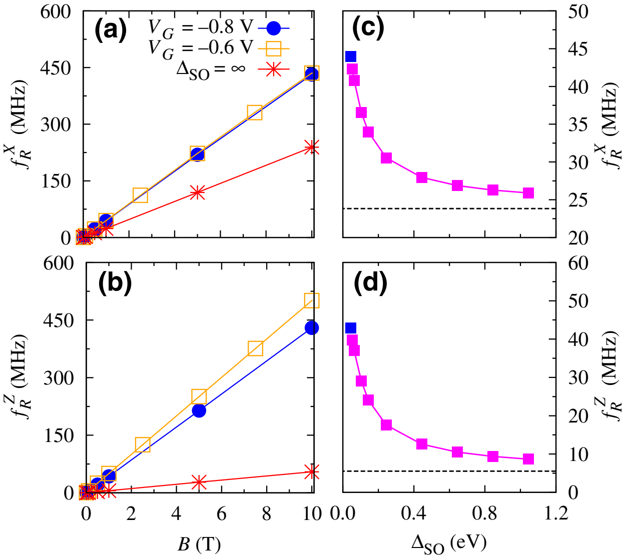

FIG. 4. The Rabi frequencies (a) f_R^X and (b) f_R^Z as a function of the magnetic field intensity B ($\theta = 45^\circ$ and $\phi = 0^\circ$). The Rabi frequencies (c) f_R^X and (d) f_R^Z as a function of Δ_{SO}, ranging from 0.044 eV (its actual value in Si, blue squares) to 1 eV ($B = 1$ T, $V_G = -0.8$ V). The limit $\Delta_{SO} = \infty$ (dotted lines) corresponds to calculations performed without including the split-off band.

case for $|1,\Uparrow\rangle$ and $|1,\Downarrow\rangle$ in the zero-field limit (see Appendix C). In order for f_R^X to take a finite value, the static magnetic field must thus mix states belonging to different Kramers doublets [45]. Such mixing is induced by the different components of the magnetic field Hamiltonian and results in a linear dependence on the field intensity for both f_R^X and f_R^Z. Here, in particular, both Rabi frequencies increase with a rate of 45 MHz/T at $B = 1$ T, for a nonoptimal orientation of the static magnetic field [Figs. 4(a) and 4(b)]. This demonstrates the possibility of efficiently manipulating the hole-spin qubits within the planar FDSOI geometry and, more specifically, in the Si scaled p-MOSFET structure that we are considering.

In the present geometry, all the introduced magnetic Hamiltonian terms and bands contribute significantly to the values of the Rabi frequencies. In fact, the values of both f_R^X and f_R^Z obtained with the inclusion of the split-off band are at least twice as large as those obtained within a four-band approach. The four-band case can be considered as the limit of the six-band case for $\Delta_{SO} \to \infty$; by artificially increasing Δ_{SO} in the six-band calculations, we see that the Rabi frequencies tend to those obtained from the four-band calculations [Figs. 4(c) and 4(d)]. The difference between the Rabi frequencies does not result from the direct contribution of the split-off band but, rather, from the enhanced mixing that this band induces between light and heavy holes (Appendix C). The contribution that comes from the sum of the paramagnetic and diamagnetic terms in the Hamiltonian is comparable, for both f_R^X and f_R^Z, to the value obtained with the Zeeman term alone (not shown).

B. Dependence of the Larmor and Rabi frequencies on the magnetic field orientation

The multiband calculations show that the Larmor frequency varies linearly with the field intensity. In such a regime, the single hole can be formally described as a two-level system within the so-called *g-matrix formalism* [20,47], which we use in the following to illustrate the dependence of the qubit properties on the field orientation and to interpolate the results of the $\mathbf{k}\cdot\mathbf{p}$ calculations. In the present case, the g matrix can be approximately written in a diagonal form (see Appendix D) and the effective qubit Hamiltonian reads

$$\mathcal{H} = \frac{1}{2}\mu_B(g_x B_x \sigma_X + g_y B_y \sigma_Y + g_z B_z \sigma_Z). \tag{9}$$

Here, the coordinate axes x, y, and z can be identified, respectively, with the directions [110], [$\bar{1}$10], and [001], $|\xi\rangle \equiv |1,\xi\rangle$ ($\xi = \Uparrow, \Downarrow$) are the hole eigenstates obtained for a magnetic field along the z direction, and the g factors depend on the gate voltage V_G. From the above qubit Hamiltonian, it follows that the Larmor frequency can be expressed as a function of the g factors, according to the expression

$$f_L = \frac{\mu_B B}{h}\sqrt{(g_x b_x)^2 + (g_y b_y)^2 + (g_z b_z)^2} \equiv \frac{\mu_B B}{h} g^*, \tag{10}$$

where g^* is the effective g factor and $\mathbf{b} = \mathbf{B}/B = (b_x, b_y, b_z) = (\sin\theta\cos\phi, \sin\theta\sin\phi, \cos\theta)$ is the unit vector that defines the field orientation. The Larmor frequency is thus maximum (minimum) for a magnetic field aligned in the direction of the largest (smallest) g_α.

The degree of anisotropy of the g tensor results from the interplay of band mixing and the magnetic Hamiltonian, including all the magnetic terms. In fact, while purely *hh* states in the presence of a Zeeman term alone would give $g_x = g_y = 0$ and $g_z = -6\kappa = 2.57$, here we find that g_z is almost twice that value and that g_x and g_y differ from zero (Table II). The predominant *hh* character of the hole ground state and the presence of a small *lh* contribution (see Table I) characterize all the considered values of the top-gate voltage, which, however, allows a certain degree of tunability of the band mixing, and thus of the g_α. In fact, decreasing values of V_G increase the strength of the vertical (z) confinement (relative to that in the x-y plane), and thus the weight of the *hh* subbands. This, in turn, results in an increase of g_z and in a decrease of g_x and g_y. Besides, we note that the Larmor frequency is mostly determined by the Zeeman Hamiltonian for a predominant in-plane component of the magnetic field, while the paramagnetic Hamiltonian contributes mostly when $\mathbf{B}$ aligns to the z direction.

TABLE II. Upper panel: the values of the principal g factors computed for two different values of the top-gate voltage V_G. Lower panel: the maxima of the Rabi frequency f_R^X (f_R^Z) and values of the angle θ that correspond to their maxima (minima). The magnetic field intensity is $B = 1$ T.

V_G (V)	g_x	g_y	g_z	g'_x (V^{-1})	g'_y (V^{-1})	g'_z (V^{-1})
-0.6	1.342	1.700	4.074	0.553	1.192	-1.209
-0.8	1.222	1.451	4.299	0.639	1.261	-1.037

V_G (V)	$\theta^X_{R,\max}$	$f^X_{R,\max}$	$\theta^Z_{R,\min}$	$f^Z_{R,\max}$
-0.6	57.1°	83.8 MHz	57.3°	83.4 MHz
-0.8	59.9°	84.3 MHz	57.3°	88.3 MHz

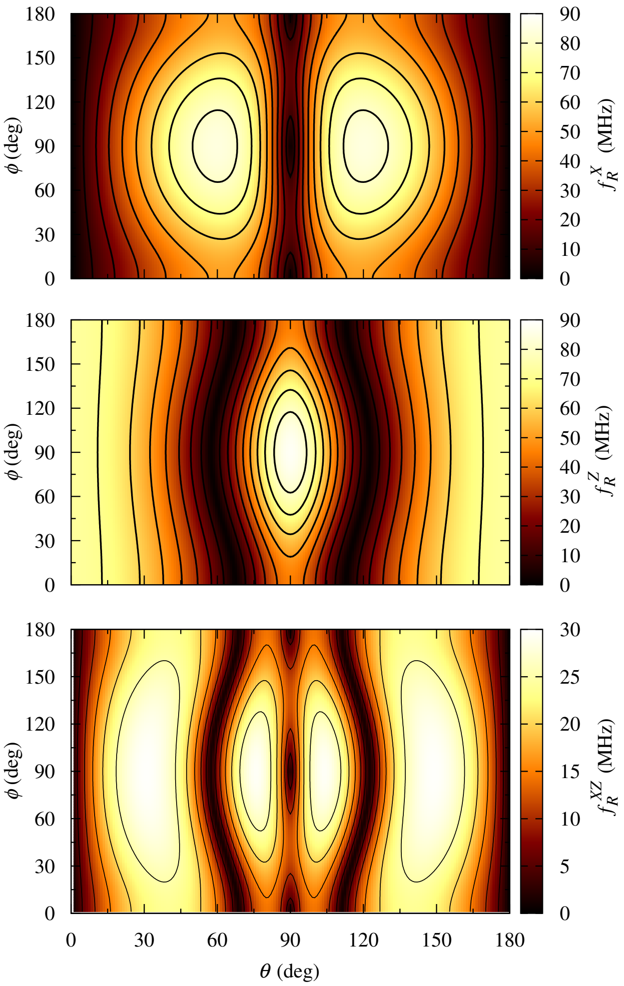

FIG. 5. The dependence of the Rabi frequencies f_R^X (upper panel) and f_R^X (middle), and of f_R^{XZ} (lower panel) on the orientation of the static magnetic field. The plotted quantities are computed by means of the g-matrix formalism ($V_G = -0.8$ V, $\delta V_G = 10$ mV, and $B = 1$ T).

The Rabi frequencies can be derived from the g tensor and its derivative with respect to the gate potential, $\hat{g}' = \partial\hat{g}/\partial V_G$ [45,48,49]. In particular, the expressions of f_R^X and f_R^X read as follows:

$$f_R^X = \frac{\mu_B B \delta V_G}{2hg^*}|(\hat{g}\mathbf{b}) \times (\hat{g}'\mathbf{b})| \tag{11}$$

and

$$f_R^Z = \frac{\mu_B B \delta V_G}{2hg^*}|(\hat{g}\mathbf{b}) \cdot (\hat{g}'\mathbf{b})|. \tag{12}$$

Our calculations show that the perturbation of the confining potential associated with the time-dependent voltages essentially preserves the symmetry of the unperturbed Hamiltonian. As a result, $\hat{g}'$ shares with $\hat{g}$ the principal axes, and the derivative of the g matrix with respect to V_G can be reduced to that of the principal g factors, the values of which are reported in Table II. Formally, this simplifies the expressions of the Rabi frequencies, since $\hat{g}'\mathbf{b} = \sum_{\alpha=x,y,z} g'_\alpha b_\alpha$. From a physical point of view, it implies that the hole manipulation can only occur through the g-tensor magnetic resonance, while the iso-Zeeman contribution to the spin-electric coupling vanishes.

The dependence of the Rabi frequencies on the orientation of the magnetic field can be derived from the above equations, once the terms g_α and g'_α have been obtained through the $\mathbf{k}\cdot\mathbf{p}$ calculations. We start by noting that the Rabi frequency f_R^X necessarily vanishes if the magnetic field is aligned along one of the principal axes. In fact, in this case, the vector $\hat{g}\mathbf{b}$ is parallel to $\hat{g}'\mathbf{b}$ and the cross product in Eq. (11) vanishes. The overall dependence of f_R^X on θ and ϕ is reported in Fig. 5 and is qualitatively similar to that obtained in different geometries [45]. The maxima of the Rabi frequency are contained in the y-z plane ($\phi = 90°$), for which one can derive an analytical expression (Appendix D). The optimal field orientation is given by [48]

$$\tan\theta^X_{R,\max} = \pm\left(\sqrt{|g_z/g_y|}\right). \tag{13}$$

The corresponding maximum of f_R^X is given by

$$f_R^{X,\max} = \frac{\mu_B B \delta V_G}{2h}\frac{\left|g_z g'_y - g_y g'_z\right|}{|g_z| + |g_y|}. \tag{14}$$

The values of $\theta^X_{R,\max}$ and $f^X_{R,\max}$ obtained in the present geometry are reported in Table II. The field orientation along the x-z plane is in general less favorable. In any case, the expressions of the optimal angle and of the maximum for $\phi = 0°$ are obtained, respectively, from Eqs. (13) and (14) by replacing y with x in the subscripts.

The dependence of the Rabi frequency f_R^Z on the magnetic field orientation is significantly different from that of f_R^X. In fact, the field orientations that maximize f_R^X yield vanishing values of f_Z^R and vice versa (Fig. 5). More specifically, as can be readily seen from Eq. (12), the optimal field direction coincides with the coordinate axis along which the derivative of the g factor is the largest:

$$f_{R,\max}^Z = \frac{\mu_B B \delta V_G}{2h} \max_{\alpha \in \{x,y,z\}} |g'_\alpha|. \tag{15}$$

In the present device geometry, this can coincide with either y or z, depending on the top-gate voltage (Table II). In any case, the optimal value of ϕ is 90°, as in the case of f_R^X. Given the analytical expression for the dependence of f_R^Z on the angle θ (Appendix D), we can also derive a simple expression for the angle at which f_R^Z vanishes, namely

$$\tan\theta_{R,\min}^Z = \pm\sqrt{\left|g_z g'_z / g_y g'_y\right|}. \tag{16}$$

As in the case of f_R^X, the expression for $\phi = 0°$ (x-z plane) can be derived from the one above by replacing y with x.

Overall, the optimal orientation of the magnetic field is one that allows the implementation of both X and Z rotations at a reasonably high Rabi frequency. Given that f_R^X and f_R^Z clearly cannot be maximized by the same field orientation, we need to identify a trade-off by maximizing a suitable figure of merit, which accounts for both rotations. A simple and yet significant option is represented by the frequency

$$f_R^{XZ} = \left(\frac{1}{f_R^X} + \frac{1}{f_R^Z}\right)^{-1} = \frac{f_R^X f_R^Z}{f_R^X + f_R^Z}. \tag{17}$$

If we identify $1/f_R^X$ and $1/f_R^Z$ with the duration of the X and Z rotations, respectively, then $1/f_R^{XZ}$ corresponds to the time required for sequentially implementing the two operations. The full dependence of f_R^{XZ} on the magnetic field orientation is reported in the bottom panel of Fig. 5. In general, its maximization is obtained for a magnetic field that lies in the y-z plane, for values of θ between those that maximize f_R^X and f_R^Z. In spite of the different angular dependencies of the two Rabi frequencies, an overall optimization can thus lead to a satisfactory trade-off. As detailed in the following section, the optimal orientation varies as a function of the channel width.

V. EFFECT OF THE CHANNEL WIDTH

The size of the devices, and specifically that of the Si channel, plays a crucial role in many respects. Smaller devices have the potential to induce a stronger quantum confinement. This results in larger energy gaps between the Kramers doublets at zero field and thus makes it possible, in principle, to use larger magnetic fields and to work at higher Larmor frequencies and possibly at higher temperatures. Besides, a change in the quantum confinement also affects the band mixing within the hole eigenstates and this unavoidably affects all the properties that have been discussed so far. In this respect, a relevant role is also played by the relative strength of the spatial confinement along the different directions. Hereafter, we focus on this latter aspect and, specifically, consider the dependence of the hole properties on the width W of the Si channel, a parameter that can be varied in the present p-MOSFETs.

A. Energy gap and band mixing

We initially analyze the dependence of the band mixing and the energy spectrum on the channel width W, which we vary from 10 to 40 nm. In particular, the energy gap ΔE between the higher logical state $|1,\Uparrow\rangle$ and the lowest noncomputational state $|2,\Downarrow\rangle$ determines the extent to which, and in which working conditions, the hole can be regarded as an effective two-level system. This applies, on the one hand, to the initialization problem, where the population leakage can result from the thermal occupation of the noncomputational states and, on the other, to the gate implementation, where the required spectral resolution and gate duration are decreasing functions of ΔE. Besides, the transition to a regime where fast qubit relaxation is induced by two-phonon (Raman, Orbach) processes occurs at temperatures that increase with the energy gap ΔE [33].

In general, ΔE is a decreasing function of the magnetic field intensity, especially if **B** is oriented along the z direction. In the presently considered system, the energy gap decreases linearly with the magnetic field intensity B [Fig. 6(a)]. However, up to $B = 10$ T, the gap remains above the value of 3 meV, corresponding to a temperature of about 34, 81 K, in the whole considered range of channel widths. This implies that the strength of the quantum confinement in the present devices would allow us to operate the qubit at a few kelvin, where reasonably high values of the decoherence times have recently been observed for similar spin qubits [22,33–37]. As far as the gate duration is concerned, the lower bound $\Delta E/\hbar$ is of the order of a few tenths of a picosecond, well above any realistic value of $1/f_R^X$.

At zero field, ΔE varies nonmonotonically with W, as reported in Fig. 6(b). In fact, the curve displays two turning points in its dependence on W, which correspond to transitions or avoided level crossings involving the ground or the first excited doublets. The minimum (at $W_a \approx 12$ nm) coincides with a nonmonotonic variation of the band-occupation probabilities for the ground state [Figs. 6(b) and 6(c)]: the occupation probability $p_{hh}^{1,\xi}$ reaches its maximum value, while it monotonically decreases for higher values of W. The opposite occurs with $p_{lh}^{1,\xi}$. The maximum

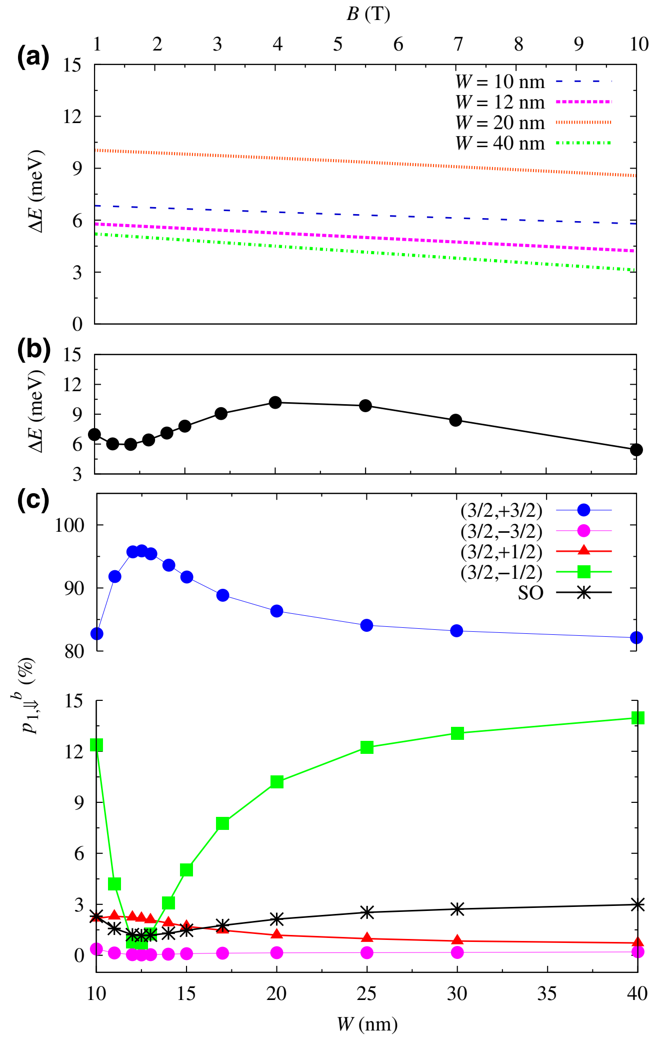

FIG. 6. (a) The energy splitting ΔE between the logical state $|1,\Uparrow\rangle$ and the lowest nonlogical state $|2,\Downarrow\rangle$ as a function of the magnetic field intensity B, for different values of the channel width W (the field is oriented along the z direction). (b) The dependence of ΔE on the channel width W at zero magnetic field and $V_G = -0.6$ V. (c) The occupation probabilities of the *lh*, *hh*, and *so* bands in the ground state in the weak-field limit ($B = 10^{-2}$ T, with $\theta = 0°$).

of ΔE (for $W_b \approx 20$ nm) coincides instead with a transition in the excited doublet, which is reflected in a change in the expectation value of σ_{yz} (not shown).

B. Larmor and Rabi frequencies

The dependence of the band mixing on the channel width is reflected in the g factors and thus in the Larmor and Rabi frequencies, which can be expressed in terms of the quantities g_α and g'_α. Strong variations of all these parameters show up at $W = W_a$ (Fig. 7). In particular, the relative change between g_z and g_y results in strong variations of the optical angle $\theta^X_{R,max}$ [see Eq. (13)], which approaches the value of 90° where g_y undergoes a sign change. Also, the optimal field orientation for the Z rotations varies from one in-plane axis to the other, due to the different dependence of g'_x and g'_y on the channel width [see Figs. 7(b) and 8(b)].

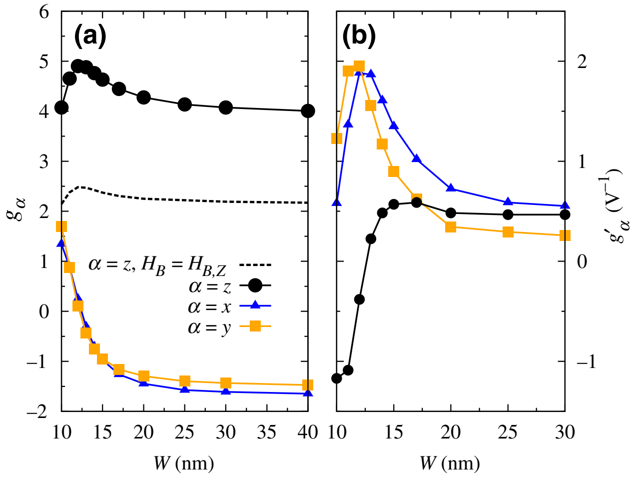

FIG. 7. The dependence on the channel width W of (a) the g factors and (b) their derivatives with respect to V_G, for $V_G = -0.6$ V. The dotted line in (a) gives the values of g_z obtained by neglecting the paramagnetic and diamagnetic contributions in the Hamiltonian ($H_B = H_{B,Z}$).

The channel width also significantly affects the dependence of the Rabi frequencies on the magnetic field orientation (Fig. 8). The values of all the maxima ($f^X_{R,\max}$, $f^Z_{R,\max}$, $f^{XZ}_{R,\max}$) display a nonmonotonic dependence on W and present a maximum for $W = W_a$, i.e., for a channel width that is slightly larger than its length $L_Q = 10$ nm. As the width approaches the value of W_a, the optimal angle $\theta^X_{R,\max}$ approaches 90° and so do $\theta^Z_{R,\max}$ and $\theta^{XZ}_{R,\max}$. Therefore, unlike what happens at larger and smaller values of W, the field orientations that allow large values of one Rabi frequency do not correspond to vanishingly small values of the other one.

VI. DISCUSSION AND OUTLOOK

The absolute values of the Rabi frequency reported above are significant in their own right, because the coupling between the spin degrees of freedom and the electric field is system dependent and cannot be taken for granted. The following step is represented by an estimate of the gate fidelity, which depends crucially on the ratio between the gating and the decoherence times. The modeling of the decoherence processes in these particular devices is beyond the scope of the present paper and measurements are still not available. However, relatively high values of the free-induction decay time (T_2^* of a few hundreds of nanoseconds) have recently been measured for hole-spin

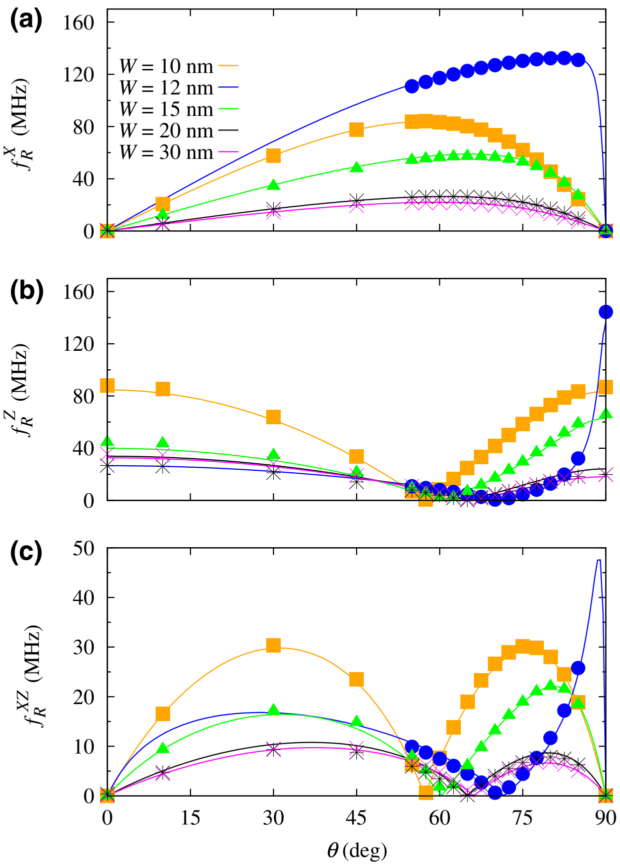

FIG. 8. The dependence on the magnetic field orientation of the Rabi frequencies (a) f_R^X, (b) f_R^Z, and (c) f_R^{XZ} for different values of the channel width W, for $V_G = -0.6$ V, $\delta V_G = 10$ mV, $B = 1$ T, and $\phi = 90^\circ$. The plots include both the results derived from the g-matrix approach (solid lines) and the numerical results obtained directly from the $\mathbf{k} \cdot \mathbf{p}$ calculations (symbols).

qubits in similar structures, with a weak dependence on the temperature in the few-kelvin regime [22].

In addition, there are specific indications that can be derived from the present results with respect to one of the main sources of decoherence for electrically driven spin qubits, namely the low-frequency electrical and charge noise. Such noise dephases the qubit by inducing random modulations of the energy gap between the logical states $|1,\Uparrow\rangle$ and $|1,\Downarrow\rangle$. The Rabi frequency f_R^Z is proportional to the qubit coupling to electrical noise (resulting from gate-voltage fluctuations) and can be regarded as a proxy for the coupling to charge noise (fluctuating charges in the vicinity of the dot will, in general, give rise to different electric field profiles and thus to different coupling constants). As shown in Fig. 5, the dependence on the magnetic field orientation of the considered Rabi frequencies is inversely correlated: in fact, the maxima of f_R^X and the zeroes of f_R^Z are approximately located in the same regions. This applies in particular to devices with a larger channel width ($W > 20$ nm), where $g_z' \approx g_y', g_x'$ and thus $\theta_{R,\max}^X \approx \theta_{R,\min}^Z$ [Eqs. (13)–(16)]. In all the considered range of channel widths, however, the zeroes of f_R^Z, which correspond to optimal operation points [50], correspond to significant values of f_R^X. This implies that if electrical noise were to represent the main source of decoherence in these devices, one could choose magnetic field orientations that suppress such coupling ($f_R^Z \approx 0$) and perform the quantum gates by combining ac-field-induced rotations around the X and Y axes only. (Rotations around the Y axis can be implemented by a $\pi/2$ shift in the phase of the oscillating field, with $f_R^X = f_R^Y$.)

An additional source of decoherence is potentially represented by phonons. In fact, the substantial spin-orbit interaction that is needed for the qubit manipulation can also result in a significant spin-phonon coupling. In a recent paper [51], Li and coworkers show that the relaxation rate of the hole-spin qubit in a Si MOSFET similar to the present one is dominated by acoustic phonons in a wide range of Larmor frequencies. Nonetheless, the phonon-limited quality factor of the Rabi oscillations can achieve a value of a few tens of thousands, for optimized bias points and magnetic field orientation. More generally, phonons can induce fast qubit relaxation at high enough temperatures, where two-phonon processes become more efficient than single-phonon transitions. In fact, while these result in a linear temperature dependence of the relaxation rate, $1/T_1$ increases as $T^7 \div T^9$ and $e^{-\Delta E/k_B T}$ for Raman and Orbach processes, respectively. However, for orbital splittings ΔE of the order of 10 meV, such as the ones that we obtain here for suitable values of the channel width W, phonons should not represent a limiting factor up to 4 K [33].

The strain and its engineering in FDSOI MOSFETs is a potentially relevant aspect and represents a field of research in its own right [52]. In particular, tensile strain along the z direction can result from the SiN hard mask used during the etching of the shallow-trench isolation regions around the device channel. Such stress strongly depends on the device geometry but tends to be negligible in scaled devices. A compressive strain in the x direction typically results from a higher Ge concentration in the *S*-*D* region compared to the channel. However, this source of strain is also absent in the present case, where both the channel and the *S*-*D* regions only contain Si. The determination of accurate strain values will require mechanical simulations and spectroscopy measurements. The impact of strain on the hole states and on the main figures of merit of the hole-spin qubits in the present devices will be the object of future research.

VII. CONCLUSIONS

In conclusion, we investigated the possibility of generating hole-spin qubits in a down-scaled Si p-MOSFET, derived from 22-nm fully depleted silicon-on-insulator

CMOS foundry technology. We find that these devices indeed allow the formation of well-defined quantum dots, for a realistic set of values of the applied (subthreshold) gate voltages. Besides, the application of time-dependent voltages to the top gate makes it possible to perform qubit rotations around two orthogonal axes, with Rabi frequencies of the order of 10^2 MHz (at 1 T). Despite the fact that the two rotations display complementary dependencies on the magnetic field orientation, good trade-offs are identified, demonstrating the possibility of efficiently implementing the two qubit rotations within the same geometry. All the relevant quantities display a strong and nonmonotonic dependence on the relative strength of the spatial confinement along the in-plane directions (the length and width of the Si channel). In particular, for a channel width that is slightly larger than its length, a clear transition is observed in the ground-state properties and is accompanied by a strong increase in the values of the maximal Rabi frequencies, which are obtained in the same range of magnetic field orientations. These results demonstrate the possibility of an all-electrical manipulation of hole-spin qubits within a FDSOI technology. Further investigation is needed in order to derive, on the one hand, the decoherence times that have to be contrasted with the above gating times and, on the other, the effect on the Rabi frequencies of the strain-integration techniques developed in CMOS technology.

ACKNOWLEDGMENTS

We acknowledge financial support from the European Commission through the IQubits project (Call H2020–FETOPEN–2018–2019–2020–01, ProjectID 829005). We acknowledge CINECA for the high-performance computing (HPC) resources and support under the Italian Supercomputing Resource Allocation (ISCRA) initiative (IsC87_ESQUDO - HP10CXQWD5).

APPENDIX A: TCAD SIMULATIONS

The confining potential $U(\mathbf{r})$ is computed using the GINESTRA TCAD software, a multiphysics and multiscale material-device simulation platform, which establishes a functional link between material properties and device electrical performance. GINESTRA relies on a kinetic Monte Carlo engine and a solid physical description of the most relevant charge transport (drift diffusion, thermoionic emission at the interface between two media and generation and/or recombination rates) and material modification mechanisms (degradation, polarization, phase change, and more) occurring during device operation. Accounting for the material properties, the doping profile, and the electrical parameters, the confining potential is computed in the whole device and then extracted in the region of interest relative to the Si channel under the gate stack (see Fig. 2). The software computes the electrostatic potential by solving the Poisson and charge-continuity equations, accounting for local electric fields, temperature, and material parameters. One major advantage in using GINESTRA is related to the capability to solve electrostatic equations even in a very low-temperature regime, reaching convergence in numerical calculations down to 1 K and below, which is the range of temperatures involved in this study. Another important feature of the GINESTRA software lies in its capability to account for a discrete description of defects that may be present in the gate stack or in other insulating regions of the device and represent an important contribution to electrostatics and transport modification (trap-assisted-tunneling). As a matter of fact, noise, variability, and reliability are generated by the presence of unwanted and unavoidable defects, which may influence the electrical properties of the device, including the quantum confining potential.

APPENDIX B: MULTIBAND CALCULATION OF THE HOLE STATES

The hole states are obtained by diagonalizing a six-band Lüttinger-Kohn envelope-function Hamiltonian $H_{\mathbf{k}\cdot\mathbf{p}}$, which accounts for the coupling between the heavy-hole ($J = |M| = 3/2$), light-hole ($J = 3/2$, $|M| = 1/2$), and split-off ($J = |M| = 1/2$) bands at the Γ point. In the basis $\{|3/2,\ 3/2\rangle\,, |3/2,\ 1/2\rangle\,, |3/2, -1/2\rangle\,, |3/2, -3/2\rangle\,, |1/2, 1/2\rangle\,, |1/2, -1/2\rangle\}$, the Hamiltonian reads as follows [43]:

$$H_{\mathbf{k}\cdot\mathbf{p}} = \begin{pmatrix} P+Q & -S & R & 0 & -S\frac{1}{\sqrt{2}} & R\sqrt{2} \\ -S^* & P-Q & 0 & R & -Q\sqrt{2} & S\frac{\sqrt{3}}{\sqrt{2}} \\ R^* & 0 & P-Q & S & S^*\frac{\sqrt{3}}{\sqrt{2}} & Q\sqrt{2} \\ 0 & R^* & S^* & P+Q & -R^*\sqrt{2} & -S^*\frac{1}{\sqrt{2}} \\ -S^*\frac{1}{\sqrt{2}} & -Q^*\sqrt{2} & S\frac{\sqrt{3}}{\sqrt{2}} & -R\sqrt{2} & P+\Delta_{\mathrm{SO}} & 0 \\ R^*\sqrt{2} & S^*\frac{\sqrt{3}}{\sqrt{2}} & Q^*\sqrt{2} & -S\frac{1}{\sqrt{2}} & 0 & P+\Delta_{\mathrm{SO}} \end{pmatrix}, \tag{B1}$$

where $\Delta_{\mathrm{SO}} = 44$ meV is the spin-orbit parameter in Si and the operators appearing in the above matrix are given by

$$P = \frac{\hbar^2}{2m_0}\gamma_1(k_x^2 + k_y^2 + k_z^2), \tag{B2}$$

$$Q = \frac{\hbar^2}{2m_0}\gamma_2(k_x^2 + k_y^2 - 2k_z^2), \tag{B3}$$

$$R = \frac{\hbar^2}{2m_0}\sqrt{3}[-\gamma_3(k_x^2 - k_y^2) + 2i\gamma_2 k_x k_y], \tag{B4}$$

$$S = \frac{\hbar^2}{2m_0}2\sqrt{3}\gamma_3(k_x - ik_y)k_z. \tag{B5}$$

The presence of a confinement potential, resulting both from the band offset in the heterostructure and from the voltage applied to the top and back gates in the p-MOSFET, is accounted for by adding the potential function $U(\mathbf{r})$ to all the diagonal elements in $H_{\mathbf{k}\cdot\mathbf{p}}$.

The presence of a static magnetic field is accounted for by the Hamiltonian term H_B. This includes the Zeeman-Bloch contribution, given by

$$H_{B,Z} = \begin{pmatrix} 3\kappa B_z & \sqrt{3}\kappa B_\phi^* & 0 & 0 & \sqrt{\frac{3}{2}}(\kappa+1)B_\phi^* & 0 \\ \sqrt{3}\kappa B_\phi & \kappa B_z & 2\kappa B_\phi^* & 0 & -\sqrt{2}(\kappa+1)B_z & \frac{1}{\sqrt{2}}(\kappa+1)B_\phi^* \\ 0 & 2\kappa B_\phi & -\kappa B_z & \sqrt{3}\kappa B_\phi^* & -\frac{1}{\sqrt{2}}(\kappa+1)B_\phi & -\sqrt{2}(\kappa+1)B_z \\ 0 & 0 & \sqrt{3}\kappa B_\phi & -3\kappa B_z & 0 & -\sqrt{\frac{3}{2}}(\kappa+1)B_\phi \\ \sqrt{\frac{3}{2}}(\kappa+1)B_\phi & -\sqrt{2}(\kappa+1)B_z & -\frac{1}{\sqrt{2}}(\kappa+1)B_\phi^* & 0 & (2\kappa+1)B_z & (2\kappa+1)B_\phi^* \\ 0 & \frac{1}{\sqrt{2}}(\kappa+1)B_\phi & -\sqrt{2}(\kappa+1)B_z & -\sqrt{\frac{3}{2}}(\kappa+1)B_\phi^* & (2\kappa+1)B_\phi & -(2\kappa+1)B_z \end{pmatrix}, \tag{B6}$$

where $B_\phi = B_x + iB_y$. Besides, we include the paramagnetic ($H_{B,P}$) and the diamagnetic ($H_{B,D}$) contributions. These come from the substitution $k_\alpha \to k_\alpha + (e/\hbar)A_\alpha$, where $\mathbf{A} = -\frac{1}{2}\mathbf{r} \times \mathbf{B}$ is the vector potential associated with the external magnetic field. The paramagnetic and diamagnetic Hamiltonians collect, respectively, the terms of order 1 and 2 in the magnetic field $\mathbf{B}$.

After the substitution of $\mathbf{k} \to -i\nabla$ in $H_{\mathbf{k}\cdot\mathbf{p}}$ and H_B, we obtain a differential Schrödinger equation, which we diagonalize in the basis $|\mathbf{n}, J, M\rangle$, where $|\mathbf{n}\rangle = |n_x, n_y, n_z\rangle$ are the eigenstates of a 3D harmonic oscillator with mass m_0/γ_1 and optimized values of the angular frequencies ω_α.

APPENDIX C: RABI FREQUENCIES

For the purposes of the following discussion, it is convenient to expand a hole eigenstate as

$$|m, \xi\rangle = \sum_b |\psi_{m,\xi}^b\rangle \otimes |b\rangle, \tag{C1}$$

where the $|\psi_{m,\xi}^b\rangle$ are the unnormalized and (in general) nonmutually orthogonal envelope functions of the hole eigenstate corresponding to the band $b = (J, M)$. At zero magnetic field, one of the two eigenstates $|m, \xi\rangle$ that belong to the mth doublet is the time-reversal conjugate of the other: $|m, \Uparrow\rangle = \Theta|m, \Downarrow\rangle$ and $|m, \Downarrow\rangle = -\Theta|m, \Uparrow\rangle$. Here, Θ is the time-reversal operator, which acts on the eigenstate components as

$$\Theta|\psi_{m,\xi}^b\rangle \otimes |J, M\rangle = (-1)^{J+M}\left|(\psi_{m,\xi}^b)^*\right\rangle \otimes \left|J, -M\right\rangle. \tag{C2}$$

Since the potential operator is diagonal with respect to the band index, we can always express the overall Rabi frequency as the algebraic sum of six contributions, each coming from a particular band:

$$f_R^X = \frac{1}{h}\left|\sum_b \langle\psi_{1,\Uparrow}^b|\delta U|\psi_{1,\Downarrow}^b\rangle\right|. \tag{C3}$$

From the above Eqs. (C1)–(C2), it follows that f_R^X vanishes identically in the zero-field limit, because the contributions (J, M) and $(J, -M)$ cancel each other.

Along the same lines, we can show that also f_R^Z vanishes identically in the zero-field limit. In fact, from Eq. (C2) and from the expression

$$f_R^Z = \frac{1}{h}\left|\sum_b \left(\langle\psi_{1,\Uparrow}^b|\delta U|\psi_{1,\Uparrow}^b\rangle - \langle\psi_{1,\Downarrow}^b|\delta U|\psi_{1,\Downarrow}^b\rangle\right)\right|, \tag{C4}$$

it follows that the terms corresponding to $\xi = \Uparrow$ and $\xi = \Downarrow$, for each (J, M), cancel each other.

Finally, the above Eqs. (C3)–(C4) allow us to estimate the way in which the band mixing affects the value of the Rabi frequencies. In particular, the direct contribution of the split-off bands is given by the terms that correspond to $b = (1/2, \pm 1/2)$. The indirect contribution of the split-off bands results instead from their effect on the mixing between the light- and heavy-hole bands in the ground states.

APPENDIX D: LARMOR AND RABI FREQUENCIES IN THE g-MATRIX FORMALISM

Within the g-matrix formalism, the effective qubit Hamiltonian reads

$$\mathcal{H} = \frac{1}{2}\mu_B \sigma \cdot \hat{g}(V_G) \cdot \mathbf{B}, \tag{D1}$$

where σ is the vector formed by the Pauli matrices. The g tensor depends on the confinement potential and thus (crucially) also on the top-gate voltage V_G. It can be derived from the expression for the hole eigenstates through the expression [45]:

$$\hat{g} = \frac{2}{\mu_B} \times \begin{pmatrix} \mathrm{Re}[\langle \Downarrow | M_x | \Uparrow \rangle] & \mathrm{Re}[\langle \Downarrow | M_y | \Uparrow \rangle] & \mathrm{Re}[\langle \Downarrow | M_z | \Uparrow \rangle] \\ \mathrm{Im}[\langle \Downarrow | M_x | \Uparrow \rangle] & \mathrm{Im}[\langle \Downarrow | M_y | \Uparrow \rangle] & \mathrm{Im}[\langle \Downarrow | M_z | \Uparrow \rangle] \\ \langle \Uparrow | M_x | \Uparrow \rangle & \langle \Uparrow | M_y | \Uparrow \rangle & \langle \Uparrow | M_z | \Uparrow \rangle \end{pmatrix}.$$

The components $M_\chi = \partial H_B / \partial B_\chi$ and the Pauli matrices are defined with respect to an arbitrary chosen reference frame and basis of hole states $\{|\Uparrow\rangle, |\Downarrow\rangle\}$ (belonging to the zero-field ground doublet). For small amplitudes of the oscillating gate potential ($|\delta V_G| \ll |V_G|$), the first derivative of the g matrix is numerically derived from the equation

$$\hat{g}'(V_G) \approx \frac{1}{\delta V_G}[\hat{g}(V_G + \delta V_G) - \hat{g}(V_G)]. \tag{D2}$$

With respect to the so-called *principal magnetic axes* and for a suitable pair of qubit basis states, the g matrix can be written in a diagonal form. Our calculations show that the principal magnetic axes approximately coincide with the crystallographic directions [110], [$\bar{1}$10], and [001], which coincide here with the coordinate axes x, y, and z. The principal g factors are derived by diagonalizing the symmetric Zeeman tensor $\hat{G} = {}^t\hat{g} \cdot \hat{g}$, which is derived from the field-induced splitting for six different field orientations [20,45]. The eigenvectors of $\hat{G}$ identify the principal magnetic axes at a given gate voltage, while the eigenvalues provide the moduli (but not the sign) of the principal g factors [53]. Here, for the calculations performed for $B = 1$ T and $V_G = -0.6, -0.8$ V, we find that the principal magnetic axes deviate from the crystallographic ones [110] (x), [$\bar{1}$10] (y), and [001] (z) by no more than 10^{-3} rad and can thus be identified with such axes.

The effective Hamiltonian can thus be expressed in terms of the g factors g_x, g_y, and g_z [Eq. (9)] and the reference states $|\Uparrow\rangle$ and $|\Downarrow\rangle$ correspond to the qubit eigenstates for a weak B field, oriented along the z axis. The general expressions given in Eqs. (11)–(12) can be simplified by assuming that the field lies along one of the coordinate planes. In particular, for $\phi = 90^\circ$ (y-z plane), the Rabi frequency corresponding to rotations around the X axis becomes

$$f_R^X(\theta) = \frac{\mu_B B \delta V_G}{2h} \frac{|g_y g_z' - g_z g_y'||\sin\theta\cos\theta|}{\sqrt{g_y^2 \sin^2\theta + g_z^2\cos^2\theta}}. \tag{D3}$$

The derivative of the above f_R^X with respect to θ vanishes for $\cos^2\theta = |g_x|/|g_x + g_z|$; hence the condition given in Eq. (13).

We can proceed along the same lines for the Rabi frequency f_R^Z. For $\phi = 90^\circ$ (y-z plane), its expression becomes

$$f_R^Z(\theta) = \frac{\mu_B B \delta V_G}{2h} \frac{|g_y g_y' \sin^2\theta + g_z g_z' \cos^2\theta|}{\sqrt{g_x^2 \sin^2\theta + g_z^2\cos^2\theta}}. \tag{D4}$$

The angles corresponding to the maximum and to the zero are readily found from Eq. (D4). The equations that describe the dependence of f_R^X and f_R^Z on the field orientation in the x-z plane are derived from the above ones by replacing g_y and g_y' with g_x and g_x', respectively.

[1] D. Loss and D. P. DiVincenzo, Quantum computation with quantum dots, Phys. Rev. A **57**, 120 (1998).

[2] F. A. Zwanenburg, A. S. Dzurak, A. Morello, M. Y. Simmons, L. C. L. Hollenberg, G. Klimeck, S. Rogge, S. N. Coppersmith, and M. A. Eriksson, Silicon quantum electronics, Rev. Mod. Phys. **85**, 961 (2013).

[3] G. Scappucci, C. Kloeffel, F. A. Zwanenburg, D. Loss, M. Myronov, J.-J. Zhang, S. De Franceschi, G. Katsaros, and M. Veldhorst, The germanium quantum information route, Nat. Rev. Mater. **6**, 926 (2021).

[4] M. Veldhorst, J. C. C. Hwang, C. H. Yang, A. W. Leenstra, B. de Ronde, J. P. Dehollain, J. T. Muhonen, F. E. Hudson, K. M. Itoh, A. Morello, and A. S. Dzurak, An addressable quantum dot qubit with fault-tolerant control-fidelity, Nat. Nanotechnol. **9**, 981 (2014).

[5] E. Kawakami, T. Jullien, P. Scarlino, D. R. Ward, D. E. Savage, M. G. Lagally, V. V. Dobrovitski, M. Friesen, S. N. Coppersmith, M. A. Eriksson, and L. M. K. Vandersypen, Gate fidelity and coherence of an electron spin in an Si/SiGe quantum dot with micromagnet, Proc. National Acad. Sci. **113**, 11738 (2016).

[6] J. Yoneda, K. Takeda, T. Otsuka, T. Nakajima, M. R. Delbecq, G. Allison, T. Honda, T. Kodera, S. Oda, Y. Hoshi,

N. Usami, K. M. Itoh, and S. Tarucha, A quantum-dot spin qubit with coherence limited by charge noise and fidelity higher than 99.9%, Nat. Nanotechnol. **13**, 102 (2018).

[7] D. M. Zajac, A. J. Sigillito, M. Russ, F. Borjans, J. M. Taylor, G. Burkard, and J. R. Petta, Resonantly driven CNOT gate for electron spins, Science **359**, 439 (2018).

[8] T. F. Watson, S. G. J. Philips, E. Kawakami, D. R. Ward, P. Scarlino, M. Veldhorst, D. E. Savage, M. G. Lagally, M. Friesen, S. N. Coppersmith, M. A. Eriksson, and L. M. K. Vandersypen, A programmable two-qubit quantum processor in silicon, Nature **555**, 633 (2018).

[9] W. Huang, C. H. Yang, K. W. Chan, T. Tanttu, B. Hensen, R. C. C. Leon, M. A. Fogarty, J. C. C. Hwang, F. E. Hudson, K. M. Itoh, A. Morello, A. Laucht, and A. S. Dzurak, Fidelity benchmarks for two-qubit gates in silicon, Nature **569**, 532 (2019).

[10] G. Zheng, N. Samkharadze, M. L. Noordam, N. Kalhor, D. Brousse, A. Sammak, G. Scappucci, and L. M. K. Vandersypen, Rapid gate-based spin read-out in silicon using an on-chip resonator, Nat. Nanotechnol. **14**, 742 (2019).

[11] D. Keith, M. G. House, M. B. Donnelly, T. F. Watson, B. Weber, and M. Y. Simmons, Single-Shot Spin Readout in Semiconductors near the Shot-Noise Sensitivity Limit, Phys. Rev. X **9**, 041003 (2019).

[12] M. Urdampilleta, D. J. Niegemann, E. Chanrion, B. Jadot, C. Spence, P.-A. Mortemousque, C. Bäuerle, L. Hutin, B. Bertrand, S. Barraud, R. Maurand, M. Sanquer, X. Jehl, S. De Franceschi, M. Vinet, and T. Meunier, Gate-based high fidelity spin readout in a CMOS device, Nat. Nanotechnol. **14**, 737 (2019).

[13] Y. Kandel, H. Qiao, S. Fallahi, G. Gardner, M. Manfra, and J. Nichol, Coherent spin-state transfer via Heisenberg exchange, Nature **573**, 553 (2019).

[14] A. Mills, D. Zajac, M. Gullans, F. Schupp, T. Hazard, and R. Petta, Shuttling a single charge across a one-dimensional array of silicon quantum dots, Nat. Commun. **10**, 1063 (2019).

[15] J. T. Muhonen, J. P. Dehollain, A. Laucht, F. E. Hudson, R. Kalra, T. Sekiguchi, K. M. Itoh, D. N. Jamieson, J. C. McCallum, A. S. Dzurak, and A. Morello, Storing quantum information for 30 seconds in a nanoelectronic device, Nat. Nanotechnol. **9**, 986 (2014).

[16] M. Veldhorst, H. G. J. Eenink, C. H. Yang, and A. S. Dzurak, Silicon CMOS architecture for a spin-based quantum computer, Nat. Commun. **8**, 1766 (2017).

[17] S. J. Pauka, K. Das, R. Kalra, A. Moini, Y. Yang, M. Trainer, A. Bousquet, C. Cantaloube, N. Dick, G. C. Gardner, M. J. Manfra, and D. J. Reilly, A cryogenic interface for controlling many qubits, ArXiv:1912.01299 (2019).

[18] X. Xue, *et al.*, CMOS-based cryogenic control of silicon quantum circuits, ArXiv:2009.14185 (2020).

[19] R. Maurand, X. Jehl, D. Kotekar-Patil, A. Corna, H. Bohuslavskyi, R. Laviéville, L. Hutin, S. Barraud, M. Vinet, M. Sanquer, and S. De Franceschi, A CMOS silicon spin qubit, Nat. Commun. **7**, 13575 (2016).

[20] A. Crippa, R. Maurand, L. Bourdet, D. Kotekar-Patil, A. Amisse, X. Jehl, M. Sanquer, R. Laviéville, H. Bohuslavskyi, L. Hutin, S. Barraud, M. Vinet, Y.-M. Niquet, and S. De Franceschi, Electrical Spin Driving by g-Matrix Modulation in Spin-Orbit Qubits, Phys. Rev. Lett. **120**, 137702 (2018).

[21] S. Bonen, U. Alakusu, Y. Duan, M. J. Gong, M. S. Dadash, L. Lucci, D. R. Daughton, G. C. Adam, S. Iordănescu, M. Păşteanu, I. Giangu, H. Jia, L. E. Gutierrez, W. T. Chen, N. Messaoudi, D. Harame, A. Müller, R. R. Mansour, P. Asbeck, and S. P. Voinigescu, Cryogenic characterization of 22-nm FDSOI CMOS technology for quantum computing ICs, IEEE Electron Device Lett. **40**, 127 (2019).

[22] L. C. Camenzind, S. Geyer, A. Fuhrer, R. J. Warburton, D. M. Zumbühl, and A. V. Kuhlmann, A spin qubit in a fin field-effect transistor, ArXiv:2103.07369 (2021).

[23] C. Kloeffel, M. Trif, P. Stano, and D. Loss, Circuit QED with hole-spin qubits in Ge/Si nanowire quantum dots, Phys. Rev. B **88**, 241405 (2013).

[24] R. Li, F. E. Hudson, A. S. Dzurak, and A. R. Hamilton, Pauli spin blockade of heavy holes in a silicon double quantum dot, Nano Lett. **15**, 7314 (2015).

[25] S. D. Liles, R. Li, C. H. Yang, F. E. Hudson, M. Veldhorst, A. S. Dzurak, and A. R. Hamilton, Spin and orbital structure of the first six holes in a silicon metal-oxide-semiconductor quantum dot, Nat. Commun. **9**, 3255 (2018).

[26] H. Watzinger, J. Kukučka, L. Vukušić, F. Gao, T. Wang, F. Schäffler, J.-J. Zhang, and G. Katsaros, A germanium hole spin qubit, Nat. Commun. **9**, 3902 (2018).

[27] A. Crippa, R. Ezzouch, A. Aprá, A. Amisse, R. Laviéville, L. Hutin, B. Bertrand, M. Vinet, M. Urdampilleta, T. Meunier, M. Sanquer, X. Jehl, R. Maurand, and S. De Franceschi, Gate-reflectometry dispersive readout and coherent control of a spin qubit in silicon, Nat. Commun. **10**, 2776 (2019).

[28] N. W. Hendrickx, W. I. L. Lawrie, L. Petit, A. Sammak, G. Scappucci, and M. Veldhorst, A single-hole spin qubit, Nat. Commun. **11**, 487 (2020).

[29] N. W. Hendrickx, D. P. Franke, A. Sammak, G. Scappucci, and M. Veldhorst, Fast two-qubit logic with holes in germanium, Nature **577**, 487 (2020).

[30] N. W. Hendrickx, W. I. L. Lawrie, M. Russ, F. van Riggelen, S. L. de Snoo, R. N. Schouten, A. Sammak, G. Scappucci, and M. Veldhorst, A four-qubit germanium quantum processor, Nature **591**, 580 (2021).

[31] S. Bosco, B. Hetényi, and D. Loss, Hole spin qubits in Si FinFETs with fully tunable spin-orbit coupling and sweet spots for charge noise, PRX Quantum **2**, 010348 (2021).

[32] S. Bosco, M. Benito, C. Adelsberger, and D. Loss, Squeezed hole spin qubits in Ge quantum dots with ultrafast gates at low power, ArXiv:2103.16724 (2021).

[33] L. M. K. Vandersypen, H. Bluhm, J. S. Clarke, A. S. Dzurak, R. Ishihara, A. Morello, D. J. Reilly, L. R. Schreiber, and M. Veldhorst, Interfacing spin qubits in quantum dots and donors—hot, dense, and coherent, npj Quantum Inf. **3**, 34 (2017).

[34] K. Ono, T. Mori, and S. Moriyama, High-temperature operation of a silicon qubit, Sci. Rep. **9**, 469 (2019).

[35] A. West, B. Hensen, A. Jouan, T. Tanttu, C.-H. Yang, A. Rossi, M. F. Gonzalez-Zalba, F. Hudson, A. Morello, D. J. Reilly, and A. S. Dzurak, Gate-based single-shot readout of spins in silicon, Nat. Nanotechnol. **14**, 437 (2019).

[36] L. Petit, H. G. J. Eenink, M. Russ, W. I. L. Lawrie, N. W. Hendrickx, S. G. J. Philips, J. S. Clarke, L. M. K. Vandersypen, and M. Veldhorst, Universal quantum logic in hot silicon qubits, Nature **580**, 355 (2020).

[37] C. H. Yang, R. C. C. Leon, J. C. C. Hwang, A. Saraiva, T. Tanttu, W. Huang, J. Camirand Lemyre, K. W. Chan, K. Y. Tan, F. E. Hudson, K. M. Itoh, A. Morello, M. Pioro-Ladrière, A. Laucht, and A. S. Dzurak, Operation of a silicon quantum processor unit cell above one kelvin, Nature **580**, 350 (2020).

[38] R. Carter, *et al.*, 22nm FDSOI technology for emerging mobile, Internet-of-Things, and RF applications, 2016 IEEE International Electron Devices Meeting, 2.2.1 (2016).

[39] Applied Materials: GINESTRA [Online]. Available:, http://www.appliedmaterials.com/products/applied-mdlx-ginestra-simulation-software.

[40] L. Vandelli, A. Padovani, L. Larcher, R. G. Southwick, W. Knowlton, and G. Bersuker, A physical model of the temperature dependence of the current through SiO_2/HfO_2 stacks, IEEE Trans. Electron Devices **58**, 2878 (2011).

[41] A. Padovani, L. Larcher, G. Bersuker, and P. Pavan, Charge transport and degradation in HfO_2 and HfO_x dielectrics, IEEE Electron Device Lett. **34**, 680 (2013).

[42] A. Padovani, D. Z. Gao, A. L. Shluger, and L. Larcher, A microscopic mechanism of dielectric breakdown in SiO_2 films: An insight from multi-scale modeling, J. Appl. Phys. **121**, 155101 (2017).

[43] L. C. Lew Yan Voon and M. Willatzen, *The $k \cdot p$ Method: Electronic Properties of Semiconductors* (Springer-Verlag, Berlin, 2009).

[44] A. Secchi, L. Bellentani, A. Bertoni, and F. Troiani, Interacting holes in Si and Ge double quantum dots: From a multiband approach to an effective-spin picture, Phys. Rev. B **104**, 035302 (2021).

[45] B. Venitucci, L. Bourdet, D. Pouzada, and Y.-M. Niquet, Electrical manipulation of semiconductor spin qubits within the g-matrix formalism, Phys. Rev. B **98**, 155319 (2018).

[46] B. Venitucci and Y.-M. Niquet, Simple model for electrical hole spin manipulation in semiconductor quantum dots: Impact of dot material and orientation, Phys. Rev. B **99**, 115317 (2019).

[47] Y. Kato, R. C. Myers, D. C. Driscoll, A. C. Gossard, J. Levy, and D. D. Awschalom, Gigahertz electron spin manipulation using voltage-controlled g-tensor modulation, Science **299**, 1201 (2003).

[48] N. Ares, G. Katsaros, V. N. Golovach, J. J. Zhang, A. Prager, L. I. Glazman, O. G. Schmidt, and S. De Franceschi, SiGe quantum dots for fast hole spin Rabi oscillations, Appl. Phys. Lett. **103**, 263113 (2013).

[49] B. Voisin, R. Maurand, S. Barraud, M. Vinet, X. Jehl, M. Sanquer, J. Renard, and S. Franceschi, Electrical control of g-factor in a few-hole silicon nanowire MOSFET, Nano Lett. **16**, 88 (2015).

[50] Z. Wang, E. Marcellina, A. R. Hamilton, J. H. Cullen, S. Rogge, J. Salfi, and D. Culcer, Optimal operation points for ultrafast, highly coherent Ge hole spin-orbit qubits, npj Quantum Inf. **7**, 54 (2021).

[51] J. Li, B. Venitucci, and Y.-M. Niquet, Hole-phonon interactions in quantum dots: Effects of phonon confinement and encapsulation materials on spin-orbit qubits, Phys. Rev. B **102**, 075415 (2020).

[52] R. Berthelon, Strain integration and performance optimization in sub-20nm FDSOI CMOS technology, Université de Toulouse (Doctoral Dissertation Thesis, 2018).

[53] L. F. Chibotaru, A. Ceulemans, and H. Bolvin, Unique Definition of the Zeeman-Splitting g Tensor of a Kramers Doublet, Phys. Rev. Lett. **101**, 033003 (2008).